Revue des Composites et des Matériaux Avancés-Journal of Composite and Advanced Materials
Vol. 36, No. 1, February, 2026, pp. 41-51
Journal homepage: http://iieta.org/journals/rcma

PANI–CQD Synergy in PVA-Based Electrolyte Membranes for Enhanced Ion Transport and Discharge Performance in Aluminium–Air Batteries

Firman Ridwan[1*], Dean Bilalwa Agusto[1], Muhammad Farid Abdullah[1], Muhammad Ilhamdi Rusydi[2], Darwison Darwison[2], Hamdi Rifai[3]

[1] Department of Mechanical Engineering, Faculty of Engineering, Andalas University, Padang 25163, Indonesia
[2] Department of Electrical Engineering, Faculty of Engineering, Andalas University, Padang 25163, Indonesia
[3] Department of Physics, Universitas Negeri Padang, Padang 25163, Indonesia

Corresponding Author Email: firmanridwan@eng.unand.ac.id

Copyright: ©2026 The authors. This article is published by IIETA and is licensed under the CC BY 4.0 license (http://creativecommons.org/licenses/by/4.0/).

https://doi.org/10.18280/rcma.360104

Received: 10 December 2025
Revised: 30 January 2026
Accepted: 15 February 2026
Available online: 28 February 2026

Keywords:
aluminium–air battery, carbon quantum dots, polyaniline, ionic conductivity, ion transport, electrolyte membrane, nanofiber separator

ABSTRACT

Aluminium–air batteries offer high theoretical energy density but are hindered by limited ionic conductivity and unstable ion transport in conventional electrolyte membranes. This study presents a synergistic material strategy integrating polyaniline (PANI)-modified polyvinyl alcohol (PVA)/HCl/tetraethyl orthosilicate (TEOS) electrolyte membranes with carbon quantum dot (CQD)-embedded polylactic acid (PLA) nanofiber separators. PANI loadings were systematically varied from 0 to 0.10 g, while CQDs synthesised from citric acid and urea were uniformly dispersed into PLA nanofibers via electrospinning. The incorporation of PANI and CQDs facilitated the formation of microporous structures and conductive pathways, as confirmed by Scanning Electron Microscope (SEM) and Fourier Transform Infrared Spectroscopy (FTIR). Electrochemical impedance spectroscopy revealed that the ionic conductivity increased from 0.453 $mS \cdot cm^{-1}$ (0 g PANI) to 1.365 $mS \cdot cm^{-1}$ (0.10 g PANI), corresponding to a 201% enhancement. The ion mobility reached 2.72×10^{-6} $cm^2 \cdot V^{-1} \cdot s^{-1}$ with a transference number of 0.82. Galvanostatic discharge tests showed that an intermediate PANI loading of 0.04 g delivered the highest discharge capacity (0.5000 mAh) and energy density (0.3750 mWh), indicating an optimal trade-off between ion transport and electrochemical utilisation. These findings demonstrate that the rational combination of PANI and CQDs provides a scalable, environmentally benign route to improve both the stability and efficiency of aluminium–air battery systems.

1. INTRODUCTION

Aluminium-air batteries are promising candidates for high-energy-density applications due to their high theoretical specific capacity and environmental compatibility. In addition to this, renewable energy reduces environmental pollution resulting from other energy production methods. These batteries could be used in portable devices and also in cars. Research has indicated that advancements in battery technology will depend on improvements to the electrolyte and separator. These components are vital to increasing battery efficiency and lifespan, and ultimately battery performance [1]. A major obstacle to the development of metal-air battery technology is the lack of a suitable air electrode, or oxidase [2]. One problem that impacts the long-term performance of Aluminum-air batteries is the degradation of the electrolyte. This occurs due to the chemical reaction between the aluminium anode and the electrolyte.

The cathode and anode are separated by battery separators to prevent the electrodes from touching each other [3]. A suitable membrane would need to be mechanically robust, possessing the strength required to withstand both the process conditions and the eventual service environment. This polymer has a high ionic conductivity [4]. The most commonly used materials in the manufacture of the electrolyte membrane are polymers, which are based on polyvinyl alcohol. This is due to the ease of modification, their environmentally friendly properties, and the fact that they are water-soluble [5, 6]. Polyvinyl alcohol (PVA) is commonly modified using tetraethyl orthosilicate (TEOS) and hydrochloric acid (HCl) to improve the membrane performance [7]. The addition of HCl allows the formation of more uniform membranes by enhancing the ionic conductivity of the complex through the formation of acid complexes. It also increases the solubility of PVA [8]. TEOS, when used as a silica precursor, is known to increase the mechanical stability, the resistance to electrochemical degradation, and the water resistance. This is as a result of a denser network of membrane forming [9]. Currently available PVA/HCl/TEOS membranes show significant drawbacks in the long-term cycling stability and electrochemical stability under the severe conditions of Aluminum-air batteries.

Conventional separators and electrolyte membranes are currently being researched in order to improve their performance by using conductive polymers and nanostructured materials. Conductive polyaniline (PANI), found in the combination of conductive polymers, significantly enhances the conductivity and stability of the electrolyte in polymer matrices [10]. Past studies have shown PANI added to such membranes can significantly boost ionic conductivity and the mechanical strength of these membranes, reduce degradation over charge/discharge cycles, and the paths by which ions move within the membrane [11]. In separator engineering, the parallel approach is used to achieve the requirements of porosity, structural stability, and high ionic conductivity, which are necessary for the operation of Aluminum-air batteries [12]. Due to its excellent ion transport characteristics and eco-friendly nature, the PLA nanofibers fabricated through electrospinning have been extensively utilised as separators [13]. The incorporation of carbon quantum dots (CQDs) into PLA nanofibres enhances the thermal stability and electronic conductivity of Aluminum-air batteries, thus improving their efficiency and durability [14]. Conductive polymers and nanomaterials, when combined, have a beneficial effect on the functioning of fuel cells, improving the performance of both the separators and the electrolytes.

Research has demonstrated that PANI and nanomaterial modifications can improve the functioning of several battery systems. A composite material based on conductive polyaniline and carbon nanotubes has been developed by Deyab et al. [15]. In order to reduce hydrogen gas evolution and corrosion of the anode in an aluminium-air battery, a small amount of silver has been added to the aluminium electrolyte. Key to the operation of the aqueous zinc ion battery is separator engineering and the intercalation of PANI [16]. Research has demonstrated that lithium-ion battery membranes with improved mechanical strength and electrical conductivity can be obtained when PANI and nanomaterials are used. Additionally, Nie et al. [17] showed that aluminum-air batteries were protected by composite membranes of polyacrylonitrile (PAN) and aluminium oxide (Al_2O_3) nanofibres. However, the combined use of PANI-modified PVA/HCl/TEOS electrolyte membranes and CQD/PLA nanofiber separators with controlled PANI loading has rarely been reported. This paper looks at the performance of aluminium-air batteries that use a CQD-PLA nanofiber separator combined with a PANI-modified PVA electrolyte. The goal of this research was to evaluate how the battery's performance was affected by the use of the new separator and electrolyte. The data gathered from the tests were used to assess the separator's performance and the electrolyte's ionic conductivity.

2. MATERIAL AND METHODS

2.1 Materials

The materials required for this study were polylactic acid (PLA) granules, which were bought from a local supplier, along with other chemicals such as dimethylformamide (DMF) and acetone (99%). CQDs were produced using a process in which urea and citric acid, both supplied by Merck, were mixed together. Chemicals required for the experiment, such as PVA, TEOS, and HCl, were brought from Sigma Aldrich, whereas PANI was acquired from the ITNANO marketplace.

2.2 Synthesis of carbon quantum dots

Through microwave-assisted synthesis methods, researchers have recently been successful in producing CQDs. 3 g of citric acid and 3 g of urea were dissolved in 10 mL of distilled water to give a uniform solution. The sample was subjected to microwave heating at a temperature range of 150 to 200℃ for 3 min. The process produced particles of CQD due to carbonisation. After undergoing the process of being heated, the particles were left to return to ambient temperature by themselves. After ensuring that the CQDs were uniformly distributed, the CQDs were added to 20 mL of DMF. Below are the procedural steps as shown in the block diagram in Figure 1.

2.3 Preparation of PLA-CQDs solution for electrospinning

The solution of electrospinning was made by dissolving 1.5 g of PLA in 6 mL of acetone, which was stirred at 60℃ for 10 min [18]. In order to complete the synthesis, 6 mL of DMF was then added, and the reaction mixture was stirred for 10 min at room temperature. Following this uniform dispersion, 4 mL of the CQD dispersion was then added, stirring at 60℃ for a further 10 min. The polymer solution was now ready for the electrospinning process, where it was subjected to a high electrical potential. Below is the process described in the flow diagram shown in Figure 1.

2.4 Electrospinning

A 10 mL solution of PLA-CQDs was loaded into a 10 mL syringe equipped with a 22-gauge needle. The syringe was then mounted onto a syringe pump, and the flow rate was set to 20 mm/min. A high voltage of 30 kV was applied, with the positive terminal connected to the needle and the negative terminal attached to the collector, which was lined with aluminium foil. The distance between the needle tip and the collector was maintained at 15 cm. After these parameters were set, electrospinning was initiated [19]. The procedural steps are illustrated in Figure 1.

2.5 Preparation of electrolyte membranes

The polymer electrolyte membrane (PEM) synthesis was a multi-step process to produce uniform products with consistent properties. PVA was first dissolved in distilled water to make a homogeneous solution. 2 g of PVA was dissolved in 100 mL of distilled water at 60℃ with stirring at 600 rpm for 50 min [20]. Following a further 30 min of stirring the mixture, 2 mL of HCI was then added to the completely dissolved PVA. Following this, stirring was continued for 30 min to ensure complete mixing of the reactants. 1 mL of TEOS was then added [21]. Upon the investigation into the influence of PANI concentration on the properties of the resultant composite, PANI was added into the solution in varying proportions of 0, 0.02, 0.04, 0.06, 0.08, and 0.10 g. The resultant solution was mixed and heated at 70℃ for 45 min to ensure a uniform dispersion. This heat treatment results in a reduction of the solution volume to 50 mL. This procedure allows for the production of a battery electrolyte solution suitable for use in Aluminum-air batteries, which is well

mixed and stable. The process is shown in the illustration of Figure 1.

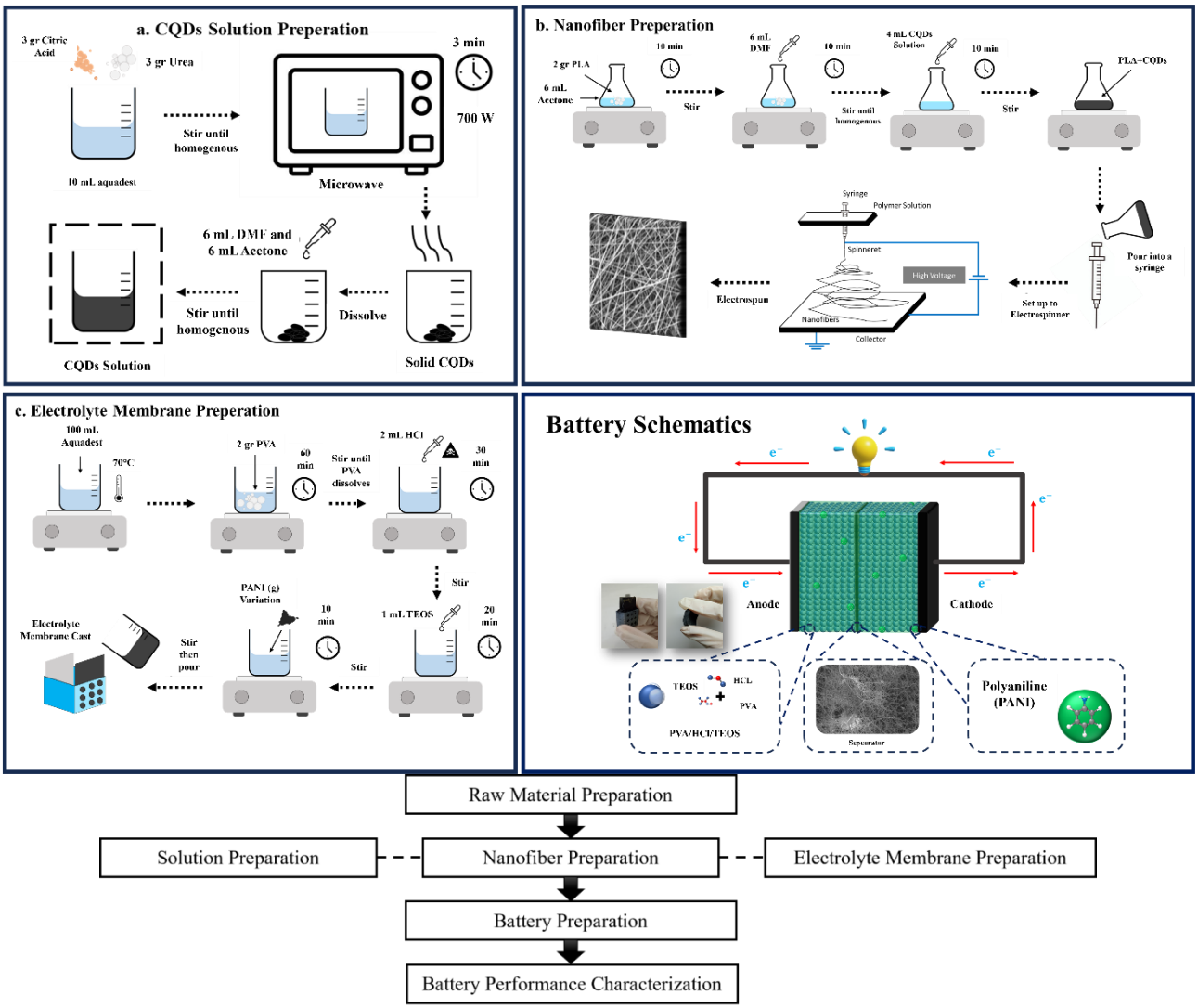

Figure 1. Aluminium-air battery preparation flowchart

2.6 Characterizations

The morphologies of the PLA-CQD fibers and electrolyte membranes were meticulously examined utilizing a Hitachi S-3400N Scanning Electron Microscope (SEM), which operates within an accelerating voltage spectrum of 200 V to 30 kV, boasts a resolution of 1.2 nm, and accommodates magnifications that extend from 10× to 1,000,000×. The SEM's functioning consists of directing an electron beam at the sample surface, resulting in the creation of signals from secondary and backscattered electrons, as well as X-rays, which are processed to achieve high-resolution imagery. These images furnish intricate insights into the structural and morphological properties of the sample. The diameters of the fibers and particles were quantified using image analysis software to determine their size distribution and precise mean dimensions [22].

The distribution of particle sizes about the constituents of the electrolyte membrane was quantitatively assessed employing a HORIBA SZ-100 Particle Size Analyzer (PSA), which operates on the principles of Dynamic Light Scattering (DLS) technology. The analysis was performed at a scattering angle of 90° and a temperature of 25.0°C, with a dispersion medium viscosity of 0.896 mPa·s. The results indicated a monodisperse distribution, ensuring precise characterization of particle size for optimal membrane performance.

Fourier Transform Infrared Spectroscopy (FTIR) was employed to identify the functional groups and molecular structures through infrared absorption, thereby facilitating the detection of compositional alterations and variations in sample purity [23]. In addition to characterizing these functional groups and molecular structures, FTIR deconvolution plays a crucial role in evaluating ion transport within the electrolyte membrane. The deconvolution methodology elucidates the proportion of free ions present within the electrolyte membrane. Consequently, the free ion percentage obtained from the FTIR deconvolution analysis was employed to approximate the density of mobile charge carriers (n), a fundamental variable in the phenomenon of ion transport. The free ion percentage and concentration of mobile charge carriers were calculated using Eqs. (1) and (2).

$$Percentage\ of\ free\ ions\ (\%) = \frac{Af}{Af + Ac + Aa} \times 100\% \quad (1)$$

$$n = \left(\frac{M \times N_A}{V_{total}}\right) \times Free\ ions\ \% \quad (2)$$

where, A_f denotes the spatial extent beneath the peak that is indicative of the free ion domain, and A_c represents the spatial extent beneath the peak that pertains to the contact ion domain. A_a indicates the spatial extent beneath the peak that is associated with the ion aggregate domain for the quantification of free ions. Regarding the concentration of mobile charge carriers, M is defined as the number of moles of HCl used in each electrolyte, N_A is Avogadro's number (6.02×10^{23}), and V_{total} is the total volume of the electrolyte membrane.

The battery capacity was assessed using a Galvanostatic Discharge Test, which evaluates the capacity (C), capacity density (CD), and energy density ($E_{density}$) of a battery or supercapacitor under constant discharge conditions. A fixed discharge current was applied to the energy storage device, and the voltage variations were recorded to determine the capacity and energy efficiency of the membrane. The capacity was calculated using Eqs. (3)-(5).

$$C = (I \times t)A \tag{3}$$

$$CD = \frac{(I \times t)A}{m} \tag{4}$$

$$E_{density} = \frac{C \times V_{avg}}{m} \tag{5}$$

In this context, I represent the current applied, t denotes the time of discharge, A refers to the anode's surface area, V_{avg} stands for the average voltage, and m indicates the mass of the anode.

Table 1. Parameter matrix table

Sample Code	PVA (g)	HCl (mL)	TEOS (mL)	PANI (g)	Mixing Temperature (℃)	Mixing Time (min)	Membrane Thickness (cm)	Separator Type	Characterization / Test Items
PHT	2.00	2.0	1.0	0.00	70	45	0.50	PLA–CQD nanofiber	SEM, FTIR, EIS, GD, TN, CV
PHT-0.02PANI	2.00	2.0	1.0	0.02	70	45	0.50	PLA–CQD nanofiber	SEM, FTIR, EIS, GD, TN, CV
PHT-0.04PANI	2.00	2.0	1.0	0.04	70	45	0.50	PLA–CQD nanofiber	SEM, FTIR, EIS, GD, TN, CV
PHT-0.06PANI	2.00	2.0	1.0	0.06	70	45	0.50	PLA–CQD nanofiber	SEM, FTIR, EIS, GD, TN, CV
PHT-0.08PANI	2.00	2.0	1.0	0.08	70	45	0.50	PLA–CQD nanofiber	SEM, FTIR, EIS, GD, TN, CV
PHT-0.10PANI	2.00	2.0	1.0	0.10	70	45	0.50	PLA–CQD nanofiber	SEM, FTIR, EIS, GD, TN, CV

Note: PHT: PVA/HCl/TEOS composite membrane; PVA: polyvinyl alcohol; HCl: hydrochloric acid; TEOS: tetraethyl orthosilicate; PLA–CQD: polylactic acid nanofibers embedded with carbon quantum dots; SEM: Scanning Electron Microscopy; FTIR: Fourier Transform Infrared Spectroscopy; EIS: electrochemical impedance spectroscopy; GD: galvanostatic discharge; TN: transference number; CV: cyclic voltammetry.

A material's ability to conduct AC is characterised by its impedance (|Z|). The impedance of a material is determined by its resistance to the flow of AC and its capacity to either hold up or supply energy in response to the change in the current. The electrochemical impedance spectroscopy (EIS) technique has been used at high voltage to examine the system over a wide range of frequencies (10 mHz to 100 kHz). The test voltage used consisted of 10 mV DC offset plus a 10 mV rms AC signal in order to assess the electrochemical properties of the device. At each frequency, the Z_{re} and Z_{im} values were recorded by the potentiostat during the measurements. The impedance was determined by the application of Eq. (6).

$$|Z| = \sqrt{Z_{re}^2 + Z_{im}^2} \tag{6}$$

The ionic conductivity of the synthesized membrane was evaluated using EIS with a Corrtest 100E potentiostat. The measurements were conducted across a frequency range of 10 mHz to 100 kHz, applying a direct current (DC) voltage of 0 mV and an alternating current (AC) voltage of 10 mV rms at room temperature. Before the measurement, the system was stabilized for approximately 10 min. The surface area of the electrolyte was 4 cm². The conductivity was calculated using Eq. (7).

$$\sigma = \frac{L}{R_{b\ X\ A}} \tag{7}$$

In this context, L represents the thickness of the electrolyte membrane, which is 0.5 cm; Rb denotes the bulk resistance, as determined by the intercept on the Nyquist plot; and A stands for the electrode area, measuring 2 cm².

By assessing the percentage of free ions and the concentration of mobile charge carriers (n), in conjunction with ionic conductivity data (σ), one can comprehensively evaluate ion mobility (μ) and the diffusion coefficient (D). This approach provides valuable insights into the ion transport characteristics of electrolyte membranes. The ion mobility (μ) and diffusion coefficient (D) can be calculated using Eqs. (8) and (9):

$$\mu = \frac{\sigma}{ne} \tag{8}$$

$$D = \frac{\mu k_b T}{e} \tag{9}$$

where, e is the electric charge (1.602×10^{-19} C), k_b is the Boltzmann constant (1.38×10^{23} J/K), and T is the absolute temperature.

Chronoamperometry was employed to measure transference numbers, aiming to identify whether ionic or electronic charge carriers were dominant in the sample variation. A steady direct current (DC) voltage of 0.1 V was applied, and the resulting current was monitored over time.

The transference number was determined using Eq. (10).

$$T_{ion} = \frac{I_T - I_S}{I_T} \quad (10)$$

The redox properties of the material were analyzed using cyclic voltammetry (CV), which measures the current response to varying applied voltages (V). This method provides insights into the oxidation-reduction behavior, electrochemical mechanisms, and material stability within the electrolyte. CV is widely used to evaluate the electrochemical performance of batteries, supercapacitors, and other energy-storage systems. Table 1 presents the parameter matrix, which contains precise formulations for all samples, process parameters, and corresponding test items.

3. RESULTS AND DISCUSSION

3.1 Results

3.1.1 Scanning Electron Microscope analysis

The morphological features of the PLA–CQD fibers and polymer electrolyte membranes were analyzed using SEM. Figure 2 displays SEM images of PLA–CQD fibers created with 4 mL of CQDs and electrolyte membranes that include 0.10g of PANI. The PLA–CQD fibers demonstrate a continuous fibrous structure with a smooth surface. Surface pores are distinctly visible along the fibers, exhibiting a relatively uniform distribution. ImageJ was used for image analysis of 50 randomly selected pores (n = 50), which revealed an average pore size of 159.89 nm. The corresponding histogram in Figure 2 illustrates the pore size distribution of the PLA–CQD fibers.

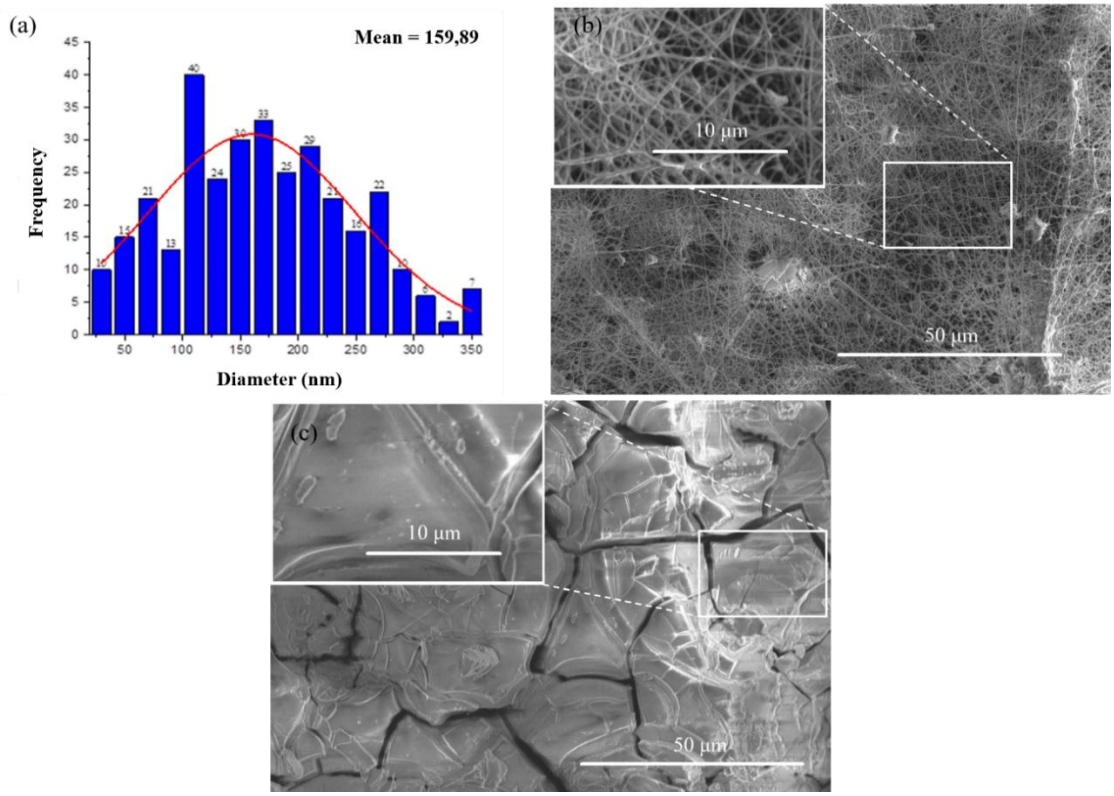

Figure 2. Scanning Electron Microscopy (SEM) images and pore size distribution of (a) pore distribution histogram, (b) Pore morphology in nanofiber, (c) morphology of polymer electrolyte membrane

SEM images of the polymer electrolyte membranes show an uneven surface morphology, marked by cracks and wavy surface features. Higher-magnification images reveal the presence of micro- and nanopores scattered across the membrane surface. Variations in surface texture and crack depth are noted in different areas of the membrane. In membranes containing PANI, alterations in surface roughness and pore structure are noticeable compared to the morphology of the PLA–CQD fibers.

3.1.2 Particle size analysis

The particle size distribution of the components in the electrolyte membrane was assessed using a laser diffraction PSA. CQDs, created from citric acid and urea, display a single-mode size distribution with a Z-average particle size of 11.0 nm and a polydispersity index (PDI) of 0.215 (n = 3). Zeta potential measurements indicate an average value of –47.6 mV, with an electrophoretic mobility of –0.000369 cm²/V·s. All measurements were conducted at 25°C in a medium with a viscosity of 0.894 mPa·s and an electrical conductivity of 0.227 mS·cm⁻¹.

3.1.3 Fourier Transform Infrared Spectroscopy

FTIR spectroscopy was employed to analyze the chemical composition of the electrolyte membranes and to identify the characteristic vibrational modes of the materials involved. Figure 3 illustrates the FTIR spectra of these membranes, emphasizing absorption bands associated with O–H stretching vibrations around 3270 cm^{-1}, C–H stretching near 2930 cm^{-1}, and the C≡C region (2000 cm^{-1}). Furthermore, the fingerprint regions show absorption bands at about 1645 cm^{-1} (C=C), 1323 cm^{-1} (C–O), and 1080 cm^{-1} (Si–O–Si). All spectra are

depicted as transmittance (%) versus wavenumber (cm^{-1}), facilitating direct comparison among various membrane compositions. These unique peaks were identified in all samples, confirming the presence of functional groups linked to the membrane components. Changes in peak intensity and band shape were noted with increasing PANI content, indicating alterations in the spectral features across the sample series. To further investigate the spectral contributions within the silica-related region, FTIR deconvolution was conducted in the wavenumber range of 850–1150 cm^{-1}, corresponding to the Si–O–Si stretching vibrations of the silica network formed within the membrane. The Si–O–Si band was broken down into several component peaks using curve-fitting analysis. Figure 4 shows the relative peak areas of these components for all membrane variations. Each spectrum includes the original FTIR curve (cyan line) along with the fitted component peaks assigned to free ions (red), contact ions (green), and ion aggregates (blue). The shaded areas indicate the relative contribution of each component to the overall spectrum. FTIR intensity is presented in arbitrary units (a.u.) as a function of wavenumber (cm^{-1}). The calculated area fraction of free ions for each sample is noted within the corresponding sub-figure. Based on the deconvolution results, the fraction of free ions across the membrane series ranges from 36.27% to 64.16%.

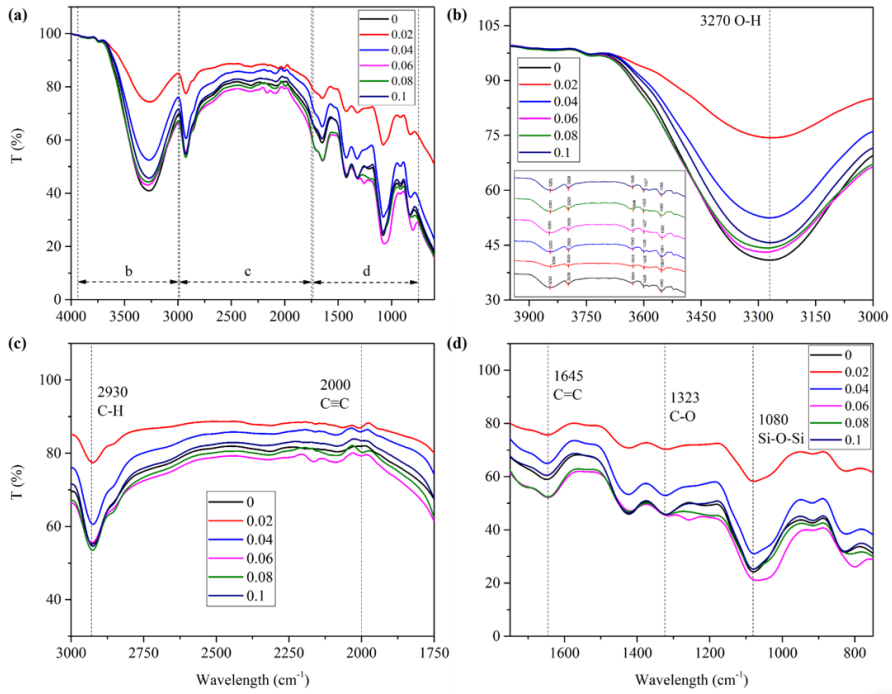

Figure 3. Electrolyte membrane Fourier Transform Infrared Spectroscopy (FTIR) spectrum of PVA/TEOS/HCl (PHT) with the addition of 0, 0.02, 0.04, 0.06, 0.08, and 0.10 g PANI: (a) 4000-600 cm^{-1}; (b) 3950-3000 cm^{-1}; (c) 3000-1750 cm^{-1}; (d) 1750-750 cm^{-1}

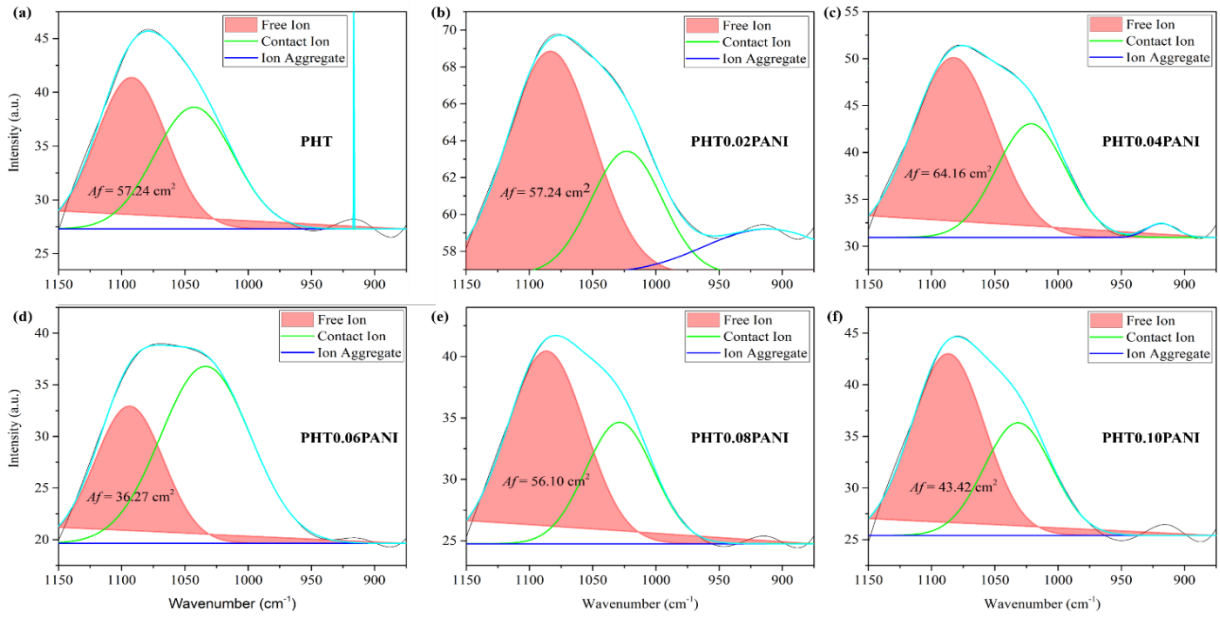

Figure 4. Fourier Transform Infrared Spectroscopy (FTIR) deconvolution plots of (a) PHT, (b) PHT0.02PANI, (c) PHT0.04PANI, (d) PHT0.06PANI, (e) PHT0.08PANI, (f) PHT0.10PANI

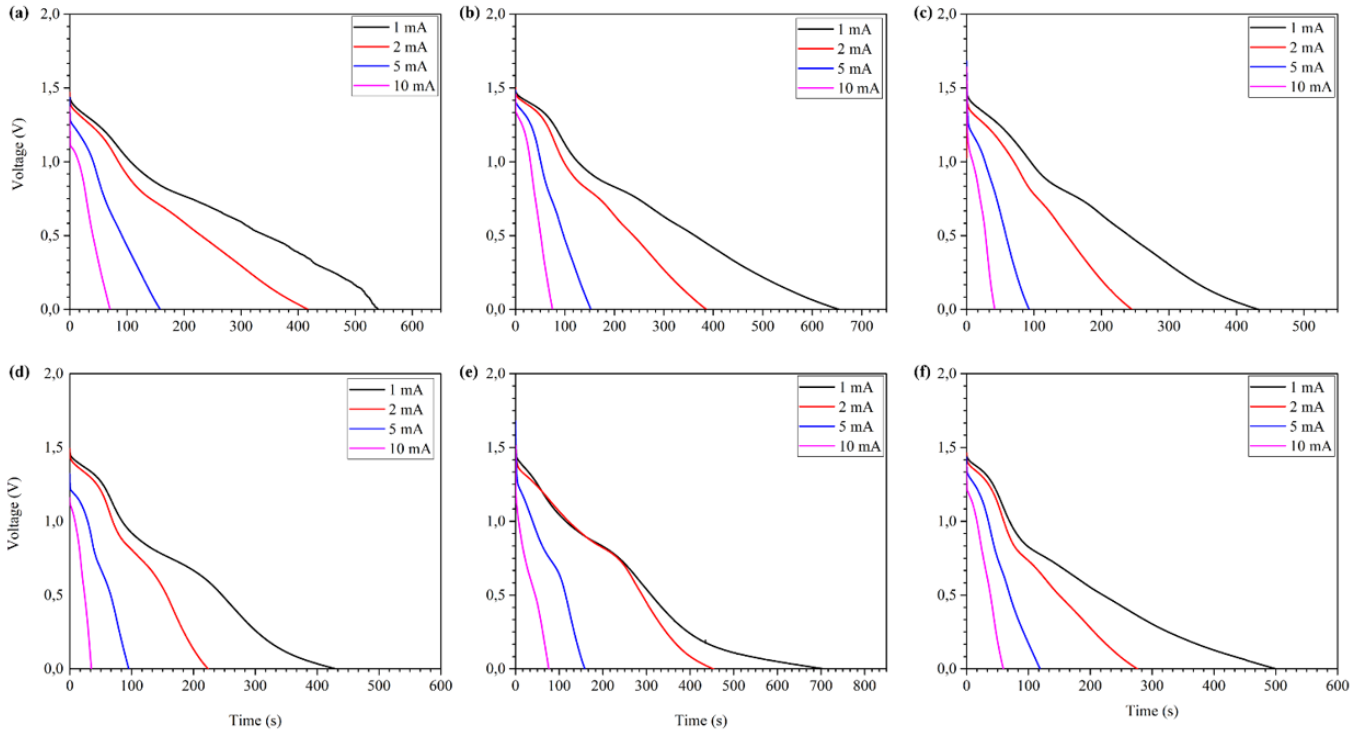

Figure 5. Battery performance during galvanostatic discharge at constant currents of 1 mA, 2 mA, 5 mA, and 10 mA and varying concentrations of PANI: (a) 0 g, (b) 0.02 g, (c) 0.04 g, (d) 0.06 g, (e) 0.08 g, and (f) 0.10 g

Table 2. Results of the galvanostatic discharge test for an aluminium-air battery utilizing a PANI-based solid polymer electrolyte

Variation	T (s)	Capacity (mAh)	CD (mAh·g^{-1})	$E_{density}$ (mWh·g^{-1})	E_{Areal} (mWh·cm^{-2})
0 g PANI	140	0.3889	0.720	0.5401	0.0729
0.02 g PANI	160	0.4444	0.823	0.6173	0.0833
0.04 g PANI	180	0.5000	0.926	0.6944	0.0938
0.06 g PANI	150	0.4167	0.771	0.5787	0.0781
0.08 g PANI	120	0.3333	0.617	0.4630	0.0625
0.10 g PANI	90	0.2500	0.463	0.3472	0.0469

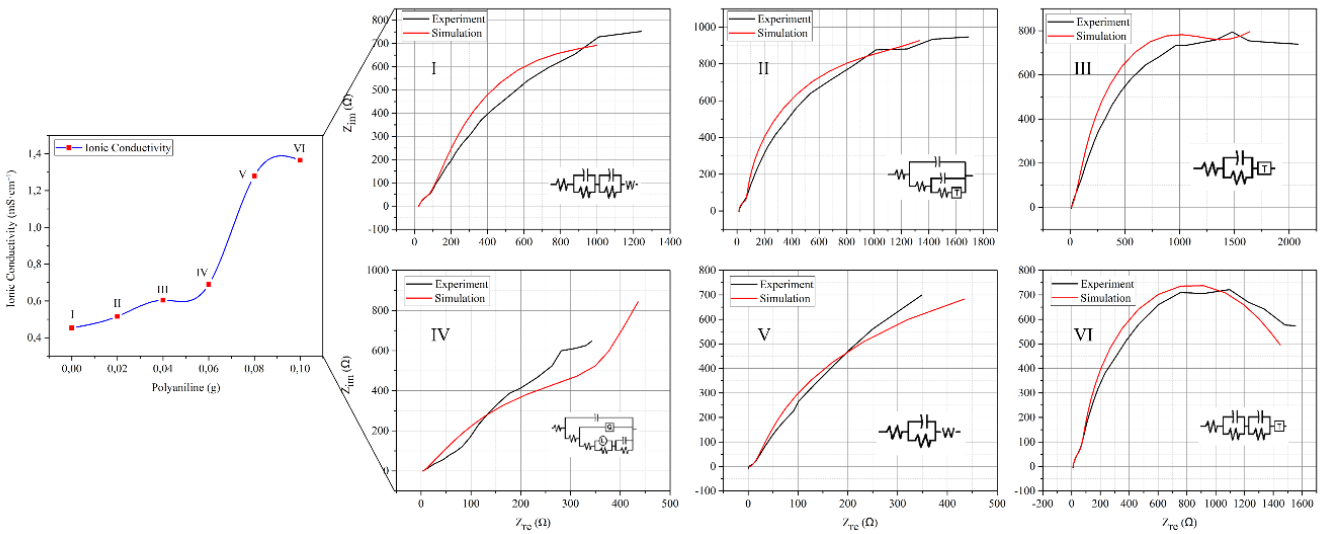

Figure 6. Graph test data, ionic conductivity diagram and impedance

3.1.4 Galvanostatic Discharge

Galvanostatic discharge tests were performed at steady currents of 1, 2, 5, and 10 mA on electrolyte membranes with varying PANI concentrations ranging from 0 to 0.10g. Figure 5 illustrates the discharge curves for each variation. Table 2 provides a summary of the discharge time, capacity, capacity density, energy density, and areal energy density obtained from these curves. The discharge capacity fluctuates between 0.2500 mAh and 0.5000 mAh, contingent on the PANI content.

Galvanostatic discharge tests indicate that samples with PANI demonstrate enhanced voltage stability during discharge. The capacity and energy density values, calculated using Eqs. (3)-(5), are presented in Table 2. The original PHT membrane (0 g PANI) achieved a discharge capacity of 0.3889 mAh and an energy density of 0.2917 mWh. Upon adding PANI, both capacity and energy density increased, peaking at 0.5000 mAh and 0.3750 mWh with a PANI content of 0.04 g.

3.1.5 Electrochemical impedance spectroscopy and ion conductivity

EIS was employed to evaluate the impedance characteristics and ionic conductivity of the electrolyte membranes under specific measurement conditions. Figure 6 displays the Nyquist plots for each membrane type, along with their respective ionic conductivity values. The recorded impedance decreases from 739.65 Ω for the membrane without PANI (0 g PANI) to 699.15 Ω for the membrane with 0.10 g PANI, showing a consistent trend across the sample series. At the same time, the ionic conductivity rises from 0.453 mS·cm^{-1} to 1.365 mS·cm^{-1} as the PANI concentration increases. To further analyze ion transport behavior, essential ion transport parameters—such as free-ion fraction, carrier density, ion mobility, diffusion coefficient, and ionic conductivity—were calculated using the relevant equations and are summarized in Table 2. These parameters provide a quantitative representation of the electrical response of the electrolyte membranes, based on the PANI content, enabling direct comparison among the various membrane compositions.

3.1.6 Transference number analysis

DC polarization measurements were employed to ascertain the ionic transference number of the electrolyte membranes. Figure 7 displays the chronoamperometry curves for all variations of the membranes. The ionic transference numbers, which were calculated, vary from 0.60 to 0.90 based on the concentration of PANI.

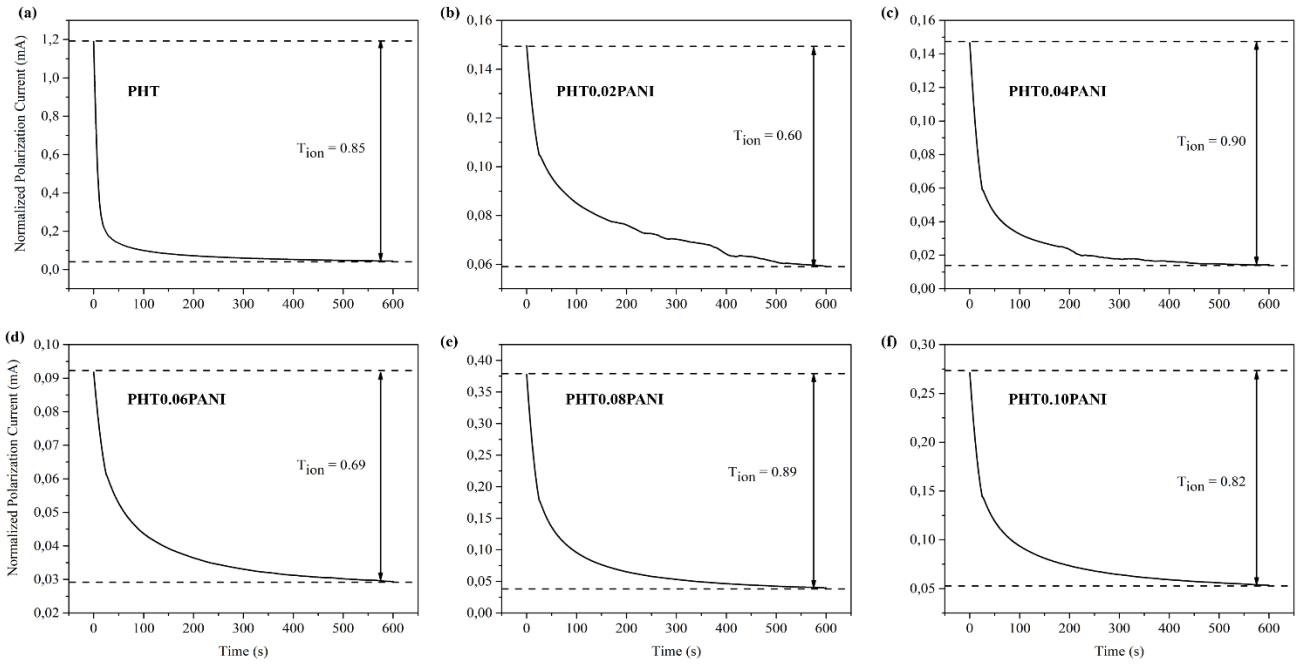

Figure 7. Chronoamperometry curves of electrolyte membranes with various PANI loadings: (a) PHT, (b) PHT0.02PANI, (c) PHT0.04PANI, (d) PHT0.06PANI, (e) PHT0.08PANI, (f) PHT0.10PANI

Table 3. Parameters of ion transport

Variation	Area of Free Ion (cm^2)	Free Ions (%)	n (Ions/cm^3)	μ (cm^2/V·s)	D (cm^2·s^{-1})	σ (mS·cm^{-1})
0 g PANI	1037.92	57.24%	4.14×10^{21}	6.83×10^{-7}	1.75×10^{-8}	0.453
0.02 g PANI	1037.92	57.24%	4.14×10^{21}	7.78×10^{-7}	2.00×10^{-8}	0.516
0.04 g PANI	1574.49	64.16%	4.64×10^{21}	8.13×10^{-7}	2.09×10^{-8}	0.604
0.06 g PANI	902.99	36.27%	2.62×10^{21}	1.64×10^{-6}	4.21×10^{-8}	0.689
0.08g PANI	1211.71	56.10%	4.05×10^{21}	1.97×10^{-6}	5.06×10^{-8}	1.280
0.1 g PANI	1276.71	43.42%	3.14×10^{21}	2.72×10^{-6}	6.98×10^{-8}	1.365

DC polarization measurements indicate that the ionic transference number changes with the PANI content, with values of 0.85 (V1), 0.60 (V2), 0.90 (V3), 0.69 (V4), 0.89 (V5), and 0.82 (V6), as depicted in Figure 7 and determined using Eq. (10). These results suggest that variations in PANI concentration significantly influence the dominant charge transport mechanism within the electrolyte system. FTIR deconvolution analysis reveals that the free-ion fraction ranges from 36.27% to 64.16% across the sample series, indicating variations in salt dissociation efficiency and ion–polymer interactions. The ionic conductivity rises from 0.453 mS·cm^{-1} for PHT0PANI to 1.365 mS·cm^{-1} for PHT0.1PANI, reflecting the combined contribution of increased charge carrier availability and enhanced ion mobility. Table 3 provides a summary of the corresponding carrier density, ion mobility, diffusion coefficient, and conductivity values, offering a

comprehensive overview of the transport properties of the investigated electrolyte membranes.

3.1.7 Cyclic voltammetry

Electrolyte membranes with different PANI levels underwent CV analysis. Figure 8 illustrates the CV curves, which display both anodic and cathodic peaks for each sample. As the PANI concentration rises, the anodic and cathodic peak currents also increase.

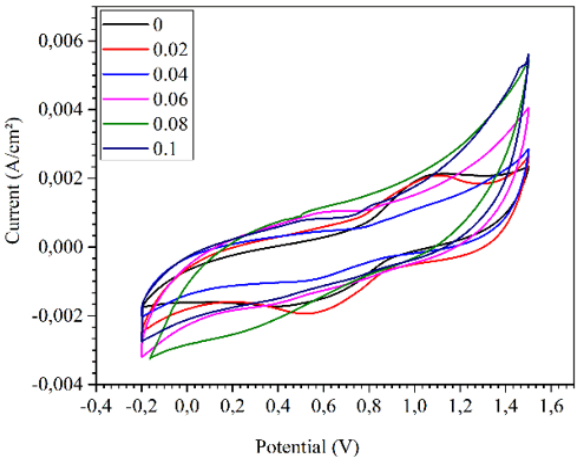

Figure 8. Cyclovoltammetry electrolyte membrane with variation of PANI

Cyclic voltammetry analysis indicates that the anodic and cathodic peak currents for the membrane lacking PANI (0 g) were around −0.00075 A and 0.00095 A, respectively. As the PANI content increased, both anodic and cathodic peak currents rose. The maximum peak currents were recorded at 0.10g PANI, reaching approximately 0.0023 A (anodic) and 0.0042 A (cathodic), as depicted in Figure 8.

3.2 Discussion

3.2.1 Scanning Electron Microscope morphology

The SEM images indicate that the pores within the CQD-PLA matrix are of nanometre dimensions. In contrast, PANI induces texture changes and cracks in the PLA film surface. By allowing pathways to connect and increasing the area over which the ions can move, these structural features enable the transport of ions. This is consistent with mechanisms of structural improvement that have been reported for polymer-based composites containing filler nanoparticles on a nanoscale. Polymer electrolyte membranes containing CQD composites have been shown to reduce the size of crystalline components, create more amorphous domains where ion transport can occur, and increase the conductivity of ions in aluminium/air fuel cells [21]. Related work has shown that adding CNTs or CQDs to a PVA membrane resulted in ionic conductivity of about 5.52-6.35 $mS \cdot cm^{-1}$. This increased conductivity is seen in modified membranes when compared with unaltered PVA but still generally follows the pattern seen in samples containing CQDs. The modifications enhance the original membrane architecture and ion transport properties to improve the stability of the ion transport.

3.2.2 Particle Size Analyzer and zeta potential

Characterisation of the CQDs indicates a very narrow size distribution of approximately 11 nm and high electrostatic stability. This high uniformity and stability are mechanistically important, as well-dispersed CQDs prevent nanoparticle aggregation and enable homogeneous distribution within the polymer matrix. Such homogeneous dispersion reduces ion-blocking domains and supports the formation of consistent ionic pathways. Previous studies have shown that incorporating conductive PANI fillers into PVA/NaCl/PANI electrolyte membranes for aluminium–air battery applications result in an ionic conductivity of about 1.69 $mS \cdot cm^{-1}$, particularly when the PANI loading is optimised to balance mechanical properties and ionic conductivity [24]. The size and stability of the CQDs are sufficient to enable a cooperative effect with PANI, while the uniform dispersion of nanofillers observed in the PSA data is critical for stable ion conduction, confirming one of the key objectives of this study.

3.2.3 Fourier Transform Infrared Spectroscopy functional groups and ion speciation

Infrared spectroscopy confirms that all of the tested membranes contained the expected chemical groups. These chemical groups are the hydroxyl (-OH), the methyl (C-H), and the silicon-oxygen-silicon (Si-O-Si). As shown in the deconvolution of the Si-O-Si region, the free-ion fraction of the counter ions changes with PANI content. These functional groups and the three-dimensional network of silicate likely enhance the dissociation of ions, which is crucial for ionic conduction. In contrast to other polymer electrolyte studies, such as those on PANI/PVDF-HFP systems, the ionic conductivity in this case is significantly higher at around 10^{-2} $mS \cdot cm^{-1}$. This is due to differences in the polymer matrix and battery type used. Nevertheless, the findings here are consistent with other research on the effect of conductive fillers and ion mobility [25]. This is achieved through the FTIR deconvolution, which is based on the research aim of determining free ions from the entire ion population in order to further investigate their transport characteristics.

3.2.4 Galvanostatic discharge performance

Electrochemical discharge experiments showed that a moderate amount of polyaniline, 0.04 g, provided the highest discharge capacity but that an excessive amount of the polymer material diminished the performance obtained. Conductive polymer matrices of PANI have been optimised such that they assist in charge transfer, without the particles becoming large enough to inhibit the movement of ions. Previous PANI-based composite membranes have shown that at the middle level of PANI, the peak capacity was reached. In the case of PVA/NaCl/PANI Aluminum-air cells, this was 0.188 mAh. The PANI content has been optimised in an effective manner so that the discharge performance can be significantly enhanced.

3.2.5 Electrochemical impedance spectroscopy and ionic conductivity

Increasing PANI concentration from 0.1 to 0.4 mol/l resulted in a decrease in impedance as determined by EIS, alongside an increase in ionic conductivity, the highest ionic conductivity being 1.365 $mS \cdot cm^{-1}$. PANI acts to form conductive pathways, which allow ions to jump from one location to another, supported by the observed increase in ion mobility despite the variable concentration of free ions. Research into polymer blends shows that the addition of conductive filler increases the pathways through which charge

is transported, even when the degree of ion separation does not increase linearly with the material's conductivity [26]. High levels of conductivity (around 6.35 $mS \cdot cm^{-1}$) were found in CQD- carbon nanotube (CNT) systems, pointing out the value of using multiple nanofillers. This backs up previous findings that adding conductive additives does enhance conductivity. The data obtained verifies the idea of lowering the resistance to the ion transport and increasing the membrane conductivity.

3.2.6 Transference number and cyclic voltammetry

Ion transference number measurements indicated predominantly ionic conductivity across all samples, with a range of the effective window from 0.04 to 0.08 g PANI. The CV behaviour indicates that as the proportion of PANI increases, the peak current also increases, which indicates that both the redox reaction and the transfer of charge are accelerated. The formation of conductive pathways in PANI is directly linked to electrochemical reactivity and ionic conductivity. In analogous composite materials made from conductive polymers, improvements in electrochemical properties were observed when their structure was optimized to enhance conductivity and structural integrity. This study helps in achieving the main goal of enhancing the electrochemical properties and the ion transport properties.

4. CONCLUSIONS

This research focused on enhancing the stability of ion transport and the electrochemical performance of aluminium–air batteries by integrating PANI-modified PVA/HCl/TEOS electrolyte membranes with CQD-embedded PLA nanofiber separators. The findings reveal that the controlled incorporation of PANI is crucial for balancing ionic conductivity, ion mobility, and discharge performance. Notably, adding 0.10 g of PANI boosted the ionic conductivity from 0.453 mS cm^{-1} to 1.365 mS cm^{-1} (an improvement of approximately 201%) and increased ion mobility to 2.72×10^{-6} cm^2 V^{-1} s^{-1} with an ionic transference number of 0.82. Meanwhile, an intermediate PANI loading of 0.04 g achieved the highest discharge capacity (0.5000 mAh) and energy output (0.3750 mWh), suggesting an optimal balance between ion transport efficiency and electrochemical utilization. Beyond these quantitative results, this study provides a material design strategy for quasi-solid-state battery components by demonstrating how conductive polymer loading and nanostructured separator engineering can be tailored to optimize ion transport pathways, electrochemical stability, and functional performance. The combined use of PANI-enhanced electrolyte membranes and CQD–PLA nanofiber separators present a scalable and environmentally friendly method for advancing aluminium–air battery technology and related metal–air energy systems. Examine the long-term cycling stability and durability of the optimized membrane–separator system under extended discharge and intermittent operation conditions. Expand the material design approach to other battery chemistries, such as zinc–air or hybrid metal–air systems, to assess its broader applicability. Assess the cost-effectiveness and scalability of membrane and separator fabrication, including considerations for large-area electrospinning and material recycling for practical deployment.

AUTHOR CONTRIBUTIONS

Firman Ridwan: Conceptualization, Methodology, Writing review and comment, and Supervision, Dean Bilalwa Agusto: Visualization and Software, Muhammad Farid Abdullah: Investigation, and Writing original draft, Muhammad Ilhamdi Rusydi: Validation, Darwison Darwison: Formal Analysis, Hamdi Rifai: Data Curation.

CONFLICTS OF INTEREST

The authors declare that they have no known competing financial interests or personal relationships that could have appeared to influence the work reported in this paper.

ACKNOWLEDGEMENTS

This research was funded by the Directorate General of Higher Education, Research, and Technology, Ministry of Education, Culture, Research, and Technology, Indonesia, based on research contract number 060/C3/DT.05.00/PL/2025, for the Fiscal year 2025.

REFERENCES

[1] Li, Z., Zhang, X., Gao, W. (2024). State of health estimation of lithium-ion battery during fast charging process based on BiLSTM-Transformer. Energy, 311: 133418. https://doi.org/10.1016/j.energy.2024.133418

[2] Suganya, R., Joseph, L.L., Kollem, S. (2024). Understanding lithium-ion battery management systems in electric vehicles: Environmental and health impacts, comparative study, and future trends: A review. Results in Engineering, 24: 103047. https://doi.org/10.1016/j.rineng.2024.103047

[3] Ji, G., He, L., Wu, T., Cui, G. (2025). The design of fast charging strategy for lithium-ion batteries and intelligent application: A comprehensive review. Applied Energy, 377: 124538. https://doi.org/10.1016/J.APENERGY.2024.124538

[4] Balaram, V., Santosh, M., Satyanarayanan, M., Srinivas, N., Gupta, H. (2024). Lithium: A review of applications, occurrence, exploration, extraction, recycling, analysis, and environmental impact. Geoscience Frontiers, 15(5): 101868. https://doi.org/10.1016/J.GSF.2024.101868

[5] Mauger, A., Armand, M., Julien, C.M., Zaghib, K. (2017). Challenges and issues facing lithium metal for solid-state rechargeable batteries. Journal of Power Sources, 353: 333-342. https://doi.org/10.1016/J.JPOWSOUR.2017.04.018

[6] Waseem, M., Lakshmi, G.S., Ahmad, M., Suhaib, M. (2025). Energy storage technology and its impact in electric vehicle: Current progress and future outlook. Next Energy, 6: 100202. https://doi.org/10.1016/J.NXENER.2024.100202

[7] Rani, B., Yadav, J.K., Saini, P., Pandey, A.P., Dixit, A. (2024). Aluminum-air batteries: Current advances and promises with future directions. RSC Advances, 14(25): 17628-17663. https://doi.org/10.1039/D4RA02219J

[8] Srivastava, S., Ahuja, D., Varshney, P.K. (2024). Impact of surface modification of electrode for aluminium air

batteries. Journal of Energy Storage, 76: 109588. https://doi.org/10.1016/J.EST.2023.109588
[9] Meng, P., Yang, Z., Zhang, J., Jiang, M., et al. (2023). Electrolyte design for rechargeable aluminum-ion batteries: Recent advances and challenges. Energy Storage Materials, 63: 102953. https://doi.org/10.1016/J.ENSM.2023.102953
[10] Saraswat, S.K., Mustafa, M.A., Ghadir, G.K., Kaur, M., Lozada, D.F.G., et al. (2024). Carbon quantum dots: A comprehensive review of green synthesis, characterization and investigation their applications in bioimaging. Inorganic Chemistry Communications, 162: 112279. https://doi.org/10.1016/J.INOCHE.2024.112279
[11] Arora, G., Sabran, N.S., Ng, C.Y., Low, F.W., Jun, H.K. (2024). Applications of carbon quantum dots in electrochemical energy storage devices. Heliyon, 10(15): e35543. https://doi.org/10.1016/J.HELIYON.2024.E35543
[12] Rani, G., Ahlawat, R., Kumar, H. (2024). Green source-based carbon quantum dots, composites, and key factors for high-performance of supercapacitors. Journal of Power Sources, 617: 235170. https://doi.org/10.1016/J.JPOWSOUR.2024.235170
[13] Shaker, M., Ng, S., Ghazvini, A.A.S., Javanmardi, S., Gaho, M.A., Jin, Z., Ge, Q. (2024). Carbon/graphene quantum dots as electrolyte additives for batteries and supercapacitors: A review. Journal of Energy Storage, 85: 111040. https://doi.org/10.1016/J.EST.2024.111040
[14] Zhang, Y.C., Briat, O., Boulon, L., Deletage, J.Y., Martin, C., Coccetti, F., Vinassa, J.M. (2019). Non-isothermal Ragone plots of Li-ion cells from datasheet and galvanostatic discharge tests. Applied Energy, 247: 703-715. https://doi.org/10.1016/J.APENERGY.2019.04.027
[15] Deyab, M.A., Mohsen, Q. (2021). Suppressing corrosion and hydrogen gas evolution in aluminum-air batteries via conductive nanocomposites. Journal of Power Sources, 506: 230171. https://doi.org/10.1016/J.JPOWSOUR.2021.230171
[16] Deng, L., Sun, K., Liu, J., Li, Z., Cao, J., Liao, S. (2024). High performance aqueous zinc-ion batteries developed by PANI intercalation strategy and separator engineering. Molecules, 29(13): 3147. https://doi.org/10.3390/MOLECULES29133147/S1
[17] Nie, X., Wu, S., Mensah, A., Lu, K., Wei, Q. (2020). Carbon quantum dots embedded electrospun nanofibers for efficient antibacterial photodynamic inactivation. Materials Science and Engineering: C, 108: 110377. https://doi.org/10.1016/J.MSEC.2019.110377
[18] Casasola, R., Thomas, N.L., Trybala, A., Georgiadou, S. (2014). Electrospun poly lactic acid (PLA) fibres: Effect of different solvent systems on fibre morphology and diameter. Polymer, 55(18): 4728-4737. https://doi.org/10.1016/j.polymer.2014.06.032
[19] Zakky, M.A., Ridwan, F., Agusto, D.B., Wismalqi, W., Gusriwandi, G. (2025). Enhancement of aluminum-air battery performance using rice husk-derived carbon quantum dots and carbon nanotubes. Journal of Fibers and Polymer Composites, 4(2): 101-119. https://doi.org/10.55043/jfpc.v4i2.403
[20] Polu, A.R., Kumar, R. (2013). Preparation and characterization of PVA based solid polymer electrolytes for electrochemical cell applications. Chinese Journal of Polymer Science, 31(4): 641-648. https://doi.org/10.1007/s10118-013-1246-3
[21] Haryadi, Sugianto, D., Ristopan, E. (2015). Development of composite membranes of PVA-TEOS doped KOH for alkaline membrane fuel cell. AIP Conference Proceedings, 1699(1): 040016. https://doi.org/10.1063/1.4938331
[22] Schneider, C.A., Rasband, W.S., Eliceiri, K.W. (2012). NIH image to ImageJ: 25 years of image analysis. Nature Methods, 9(7): 671-675. https://doi.org/10.1038/nmeth.2089
[23] Griffiths, P.R., De Haseth, J.A. (2007). Fourier Transform Infrared Spectrometry. John Wiley & Sons.
[24] Ridwan, F., Husin, M.A. (2025). Effect of polyaniline on the ionic conductivity of PVA/NaCl composite electrolyte membranes. ASEAN Journal of Chemical Engineering, 25(2): 198-206. https://doi.org/10.22146/ajche.13878
[25] Ahmad, A.L., Farooqui, U.R., Hamid, N.A. (2018). Porous (PVDF-HFP/PANI/GO) ternary hybrid polymer electrolyte membranes for lithium-ion batteries. RSC Advances, 8(45): 25725-25733. https://doi.org/10.1039/C8RA03918F
[26] Tara-Lunga-Mihali, M., Plesu, N., Macarie, L., Iliescu, S., Ilia, G. (2014). Polyaniline composite designed for solid polymer electrolyte. Pure and Applied Chemistry, 86(11): 1853-1860. https://doi.org/10.1515/pac-2014-0605